The Ice Chemistry in Comets and Planet-forming Disks: Statistical Comparison of CH3OH, H2CO, and NH3 Abundance Ratios

Manuela Lippi, Linda Podio, Claudio Codella, Sara Faggi, Marta de Simone, Geronimo L. Villanueva, Michael J. Mumma, Cecilia Ceccarelli

The Astrophysical Journal Letters, 970:L5 (14pp), 2024 July 20 https://doi.org/10.3847/2041-8213/ad5a6d

The Ice Chemistry in Comets and Planet-forming Disks: Statistical Comparison of CH_3OH, H_2CO, and NH_3 Abundance Ratios

Manuela Lippi[1], Linda Podio[1], Claudio Codella[1], Sara Faggi[2,5], Marta De Simone[3], Geronimo L. Villanueva[2], Michael J. Mumma[2], and Cecilia Ceccarelli[4]
[1] INAF—Osservatorio Astrofisico di Arcetri, Largo Enrico Fermi 5, 50125 Firenze, Italy; manuela.lippi@inaf.it
[2] NASA—Goddard Space Flight Center, 8800 Greenbelt Rd., Greenbelt, MD 20771, USA
[3] ESO, Karl Schwarzchild Str. 2, D-85478 Garching bei München, Germany
[4] Univ. Grenoble Alpes, CNRS, IPAG, F-38000 Grenoble, France
[5] American University, 4400 Massachusetts Ave NW, Washington, DC 20016, USA
Received 2024 May 10; revised 2024 June 18; accepted 2024 June 20; published 2024 July 11

Abstract

Comets are frozen remnants of our solar system's formation, and comparing their chemical composition to that of planet-forming systems can reveal crucial insights about our origins, potentially answering one of the most challenging questions in planetary science, i.e., whether cometary material was mainly inherited from the protosolar nebula or reprocessed during the solar system formation. Here we provide the first statistical analysis of methanol, formaldehyde, and ammonia abundances in 35 comets and 11 protostellar solar analogs and planet-forming disks. We show that comets from different dynamical families have comparable compositions on average, implying that their chemistry is preserved even after formation. While abundances retrieved from infrared and (sub)millimeter ground-based observations are in agreement, there are significant differences with those obtained via mass spectroscopy for 67P/Churyumov–Gerasimenko, target of the ESA-Rosetta mission; we discuss the implication of relying solely on the latter data for comparisons with disk abundance ratios. Finally, we find a significant difference in the $[CH_3OH]/[H_2CO]$ ratio in comets observed within or farther than 1 au from the Sun, suggesting that temperature-activated mechanisms can enhance the H_2CO production in the coma; this bias can strongly influence our understanding of comet chemistry in the context of planet formation. When compared to planet-forming systems, the $[CH_3OH]/[H_2CO]$ and $[NH_3]/[CH_3OH]$ molecular abundance ratios in comets are consistent with those measured in Class 0 hot corinos and in the inner regions of Class II disks, hence suggesting an inheritance scenario.

Unified Astronomy Thesaurus concepts: Chemical abundances (224); Abundance ratios (11); Comets (280); Comet origins (2203); Comet volatiles (2162); Planet formation (1241); Solar system formation (1530)

1. Introduction

Comets formed from the icy and dusty material in our protoplanetary disk approximately 4.6 billion years ago. As predicted by dynamical modeling, soon after formation they were scattered and stored in two major reservoirs: the Oort Cloud (OC), considered the primary source of long-period (LP), dynamically new (DN), and Halley-type (HT) comets, and the scattered disk of the Kuiper Belt, the main source of short-period, i.e., Jupiter-family (JF) and Encke-type (ET), comets (Gomes et al. 2005; Brasser & Morbidelli 2013; Morbidelli & Rickman 2015). Once in their reservoirs, comets' nuclei remained largely frozen until nowadays, and despite cosmic-ray bombardment and solar wind particles that might have affected the surface composition, it is believed that most of the original inner chemical composition is preserved. Understanding the composition of comets thus provides key insights into the physical, chemical, and evolutionary processes that shaped our and other planetary systems, including the degree of the chemical reprocessing in the disk (inherited or reset scenarios; Mumma & Charnley 2011; Ceccarelli et al. 2014; Eistrup et al. 2018, 2019). High-resolution spectroscopy of comets at infrared (IR) and submillimeter wavelengths has shown a high level of chemical complexity for these bodies (Dello Russo et al. 2016; Bockelée-Morvan & Biver 2017; Lippi et al. 2021). To understand the origin of this complexity and link the observed cometary composition to the stages of planetary formation, it is imperative to compare the composition of comets to that of planet-forming systems, i.e., young Sun-like stars with ages ranging from 10^4 yr (Class 0 sources) to 10^5–10^7 yr (Class I and II sources) (see, e.g., Eistrup et al. 2019; Lippi et al. 2021; Ceccarelli et al. 2023).

Recent studies on the abundance ratios of selected interstellar complex organic molecules (iCOMs; saturated C-bearing organic species with at least six atoms, of which at least one is a heavy element; Herbst & van Dishoeck 2009; Ceccarelli et al. 2017, 2023) in comets and Sun-like star-forming regions suggest interesting links. Drozdovskaya et al. (2019) show good agreement between the composition of Class 0 protostar IRAS 16293–2422 B at 60 au scale (Jørgensen et al. 2016) and that of comet 67P/Churyumov–Gerasimenko (hereafter 67P) measured with the Rosina mass spectrometer on board the ESA-Rosetta space mission (Rubin et al. 2019). Bianchi et al. (2019) find consistency between the relative abundances of formaldehyde, methanol, and iCOM species measured with IRAM 30 m in the binary Class I protostellar system SVS13-A and those reported for three comets: 67P (Le Roy et al. 2015), C/1995 O1 (Hale-Bopp), and C/2014 Q2 (Lovejoy) (Biver et al. 2015, and references therein). Podio et al. (2020) expand the sample of planet-forming systems to 11

objects, but for comparisons the authors only take into account the same three comets as in Bianchi et al. (2019). Finally, in the recent review from Ceccarelli et al. (2023), the abundance ratios of COMs with respect to methanol observed in two spatially resolved (down to 10 au) disks, HH 212 (Lee et al. 2019a, 2022) and FUor V883 Ori (Lee et al. 2019b), are compared (once more) only with C/1995 O1 (Hale-Bopp) and C/2014 Q2 (Lovejoy) (Biver et al. 2015, and references therein), finding similar values within an order of magnitude. However, these comparisons are still limited to a small number of targets and might not accurately represent the comet and disk populations, introducing interpretive biases. With the fast-increasing number of observed and well-characterized comets and protoplanetary disks, a more statistical approach is required and can now be adopted.

In this Letter, we present for the first time the statistical comparison of the abundances of methanol, formaldehyde, and ammonia and their ratios in a sample of 35 comets and 11 planet-forming systems observed with a resolution of $\leqslant$500 au. Our research intends to (i) look for significant differences between comets' dynamical classes (e.g., JF/short-period vs. OC/LP comets) that could be linked to disk processes and/or comet material evolution after storage; (ii) investigate whether 67P, frequently used for comparisons, is indicative of the average composition measured in other comets; and (iii) explore the differences in molecular abundance ratios between comets and disks/inner protostellar regions to determine whether comets did in fact inherit their chemical composition from the early stages of star formation (i.e., from Class 0 protostars of 10^4 yr), or whether a chemical reprocessing in the disk is shaping their final composition.

2. Gas-phase Molecules as Probes of the Ice Composition

The composition of interstellar ices can be inferred through the absorption features in the IR spectra of protostellar sources. Observations taken with space telescopes, first with Infrared Space Observatory (ISO) and Spitzer and more recently with the James Webb Space Telescope (JWST), allowed determining the column density and abundance of the most abundant molecules in ices, e.g., H_2O, CO, NH_3, and CH_4, as well as small COMs, such as CH_3OH (e.g., Boogert et al. 2015). The relative abundances of those species, however, are affected by large uncertainties, as the depth and shape of the absorption features depend on the methodology adopted to subtract the continuum (e.g., Bottinelli et al. 2010).

Alternatively, the ice composition may be inferred from the emission lines of gas-phase molecules that evaporate from the dust grain mantles during the warm ($T > 100$ K) protostellar phase or in the inner disk region (see, e.g., Ceccarelli et al. 2023). In this Letter, we focus on the ice composition as estimated adopting the latter approach, and we report, for completeness, the recent measurement of the ice composition in a low-mass star-forming cloud derived from absorption spectra obtained with the JWST (McClure et al. 2023).

In particular, in order to perform a statistical comparison of the ice composition in comets and planet-forming systems, we specifically focus, among other species, on methanol (CH_3OH), formaldehyde (H_2CO), and ammonia (NH_3). The relative abundances of these three molecules are indeed considered crucial indicators of ice composition, chemical processing, and physical conditions (e.g., temperature gradients) in the disk and are readily detected through gas-phase emission lines both in comets and in the circumstellar regions around young solar analogs (either in the so-called hot corino region[6] or in the inner disk; e.g., Ceccarelli et al. 2023). Methanol is considered a reliable probe of the ice composition, as it only forms on grain surfaces at low temperatures via CO freezeout and subsequent hydrogenation reactions (Watanabe & Kouchi 2002; Rimola et al. 2014; Song & Kästner 2017). Once formed, CH_3OH is released in gas phase when the dust temperature is larger than its sublimation temperature, $T_{evp}(CH_3OH) \sim 60$–130 K (e.g., Ferrero et al. 2020; Minissale et al. 2022). While methanol formation is tied to surface ice-grain chemistry, formaldehyde and ammonia can form both in gas phase and on the surface of dust grains, due to hydrogenation of CO and N (Rimola et al. 2014; Song & Kästner 2017; Jonusas et al. 2020; Tinacci et al. 2022). Their sublimation temperature, however, is lower than the one for methanol (Ferrero et al. 2020; Tinacci et al. 2022); therefore, if the observations probe a region where the dust temperature is larger than $T_{evp}(CH_3OH) \sim 60$–130 K, H_2CO and NH_3 are also expected to be released in gas phase. Under these conditions, and assuming that gas-phase reactions do not change their initial ice mixing ratios, the relative abundances of CH_3OH, H_2CO, and NH_3 are expected to be dominated by sublimation from the dust mantles, making them a good proxy of the ice composition.

3. Comets

3.1. Database and Methodology

To build our comet sample, we extracted data relative to 18 comets from the database of 20 presented in Lippi et al. (2021) (we excluded C/1999 S4 (LINEAR) and C/2012 S1 (LINEAR) since they have mostly upper limits for the selected molecules), and we added 15 more comets recently observed in the near-IR range ($\approx$3–5 μm). In addition, we included data for 13 comets studied in the spectral window between 1 and 3 mm (e.g., Biver et al. 2006, 2015). Because the same comet can be investigated at both IR and (sub)millimeter wavelengths, the two samples overlap, for a total of 35 objects. Molecular production rates in comets (i.e., the number of molecules released per second from the nucleus) are estimated from measured column densities assuming a constant rate and radial expansion at constant velocity (Haser model; Haser 1957); more details on retrieval methodologies can be found in Bockelée-Morvan et al. (2004), Bonev (2005), Lippi (2010), Villanueva et al. (2011, 2018, 2022), and Biver et al. (2022b). Molecular abundances are then usually expressed in terms of mixing ratios with respect to water, i.e., as the ratio between their production rate and that measured for water. The complete list of the comets and related references, together with the mixing ratios with respect to water of CH_3OH, H_2CO, and NH_3 and the $[CH_3OH]/[H_2CO]$ and $[NH_3]/[CH_3OH]$ abundance ratios, are reported in Appendix A.

We explored statistically this database by computing the median and standard deviation of the mixing ratio of each molecule (excluding upper limits) over the entire sample, as well as over selected subsamples, as follows. To determine whether the mixing ratios vary with heliocentric distance, we divided the comets between those observed within 1 au of the Sun and those observed farther out: in this case, we additionally

[6] Hot (>100 K), compact (<100 au), dense (>10^7 cm^{-3}) regions rich in iCOMs, where the chemistry is dominated by the ice mantle sublimation (Ceccarelli 2004).

investigated any bias between the IR and (sub)millimeter data sets. Next, we examined the median values obtained for three distinct dynamical families (DN, LP, and JF) to probe whether evolutionary processes can alter the composition of comets after their formation. Finally, we explored possible discrepancies between pre- and post-perihelion abundances, to check for additional observational biases.

In this Letter we further compare our sample with the abundances measured in 67P with the ROSINA DFMS mass spectrometer on board Rosetta, measured pre- and post-perihelion during the overall spacecraft flyby and reported by Läuter et al. (2020). From this online data set we removed mixing ratios calculated at heliocentric distances larger than 3 au, since they may be overestimated owing to inactivity (and thus underestimation) of water.

The overall statistics are reported in Table 1 and shown using box plots in Figure 1. In Figure A1 we display the mixing ratios as a function of the heliocentric distance, and in Table B1 we report the results of the two-sample Kolmogorov–Smirnov tests.

3.2. Statistical Results for the Selected Molecules

–CH_3OH: Methanol is easily measured in comets from the ground, in both the IR and (sub)millimeter wavelength ranges, showing good agreement between the two spectral ranges (see Table B1). Considering the overall database, mixing ratios with respect to water of CH_3OH in comets range from about 0.4% to 5.6%, with a median value of 2.3%. Figure 1 shows that comets observed at heliocentric distances smaller than 1 au tend to display slightly lower abundances of methanol, but the difference is not statistically relevant. Nevertheless, the number of comets observed within 1 au is low compared to the total sample (14 vs. 46), and this effect needs to be further investigated with dedicated observations. Comets from different dynamical families show on average similar CH_3OH abundances, with JF comets displaying a higher dispersion and some of the lowest values, a potential signature of different formation sites or different evolution post-formation for this class of comets. Finally, on average, we do not see large differences between pre- and post-perihelion measurements.

–H_2CO: Formaldehyde emissions are regularly observed in the IR and (sub)millimeter. In comparison to methanol, there are fewer IR measurements of H_2CO abundances, due to fainter emission lines in the spectra. At (sub)millimeter wavelengths, this molecular species is frequently seen as both a primary (i.e., released from the nucleus) and an extended (i.e., produced in the coma) source, and abundances are often reported using two different scale lengths. For consistency, in our study we considered only primary-scaled values, as is assumed in the IR. H_2CO in comets is less abundant than CH_3OH, with mixing ratios relative to water ranging from about 0.05% to 0.7%, with a median value of 0.15%. Figure 1 and the Kolmogorov–Smirnov test p-values in Table B1 show that the median mixing ratios retrieved from observations at different wavelengths, as well as for different dynamical classes, and pre- and post-perihelion are consistent within the dispersion of the data. On the other hand, there is a small disagreement between abundances calculated in comets observed at heliocentric distances smaller or larger than 1 au (p-value $\approx$ 0.08), with the latter showing on average half the value (0.3% vs. 0.15%, respectively). The excess of formaldehyde at $R_h < 1$ is most likely due to temperature-activated processes that may allow the release and disruption of a different H_2CO source, such as polymeric formaldehyde (Fray et al. 2006).

–NH_3: Ammonia can be detected in the IR, although only a few faint lines are normally seen in the spectra, resulting in a lower sample size compared to methanol and formaldehyde; moreover, we could find only one measure in the (sub) millimeter spectral region, obtained with the Herschel satellite at 572 GHz (i.e., 10P/Tempel 1; Biver et al. 2012). Considering our database, NH_3 molecular abundances range from 0.16% to 1.86%, with a median value of 0.68%. Also in this case, values relative to different dynamical types are consistent, suggesting that all comets most likely share the same original composition. Pre-perihelion abundances appear to have slightly larger values than post-perihelion ones, but the median values (0.7% vs. 0.6%, respectively) are still comparable within the dispersion (p-value larger than 0.05; see Table B1). Based on the available data, it is not possible to determine whether ammonia mixing ratios exhibit a heliocentric dependency similar to that of formaldehyde.

3.3. Comparisons with Rosetta Measurements of 67P

If we consider Figure 1 and the Kolmogorov–Smirnov test results in Table B1, the molecular abundances of CH_3OH, H_2CO, and NH_3 in 67P/Churyumov-Gerasimenko measured during the ESA-Rosetta mission flyby (Läuter et al. 2020) differ significantly from the database as obtained with ground-based observations. In addition, the Rosetta measurements display a large discrepancy between pre- and post-perihelion values for all three species.

Methanol measurements from Rosetta in 67P show on average much lower relative abundances ($\approx$0.2% and 0.9% for the pre- and post-perihelion measurements, respectively) compared to our database median value (2.31%). Nevertheless, these values are in agreement with those of $0.58\% \pm 0.10\%$, $0.86\% \pm 0.14\%$, and $0.65\% \pm 0.12\%$ reported by Bonev et al. (2023), who observed 67P with NIRSPEC-Keck in 2021. The (sub)millimeter measure of $1.2\% \pm 0.1\%$ reported in Biver et al. (2023) is slightly higher than the Rosina one, but the authors also report a water production rate derived from Odin and Nançay observations that is around half that reported by Läuter et al. (2020). The agreement between 67P ground-based observations and Rosina/Rosetta measurements strongly supports a real methanol depletion in this comet, which may have a native or evolutionary origin.

Opposite to methanol, formaldehyde in 67P observed by Rosetta displays much higher mixing ratios with respect to water than the average measured in comets by ground-based spectroscopy (0.33% and 0.55% for the pre- and post-perihelion measurements, respectively, vs. 0.15% in our sample). A reasonable interpretation is that the Rosina mass spectrometer is measuring an excess of H_2CO, most likely originating from a separate source (Fray et al. 2006; Biver et al. 2023).

Ammonia median abundances in 67P range from 0.38% to 0.18% for pre- and post-perihelion measurements, respectively, in contrast with a median value of 0.68% that we measure in other comets. This disparity, coupled with the methanol one, suggests that 67P may be a comet that has lost part of its organics. Alternatively, this comet formed in a region of the disk where NH_3 and CH_3OH could not form efficiently, i.e., in warm ($T > 30$ K) regions where the hydrogenation process is expected to be less effective.

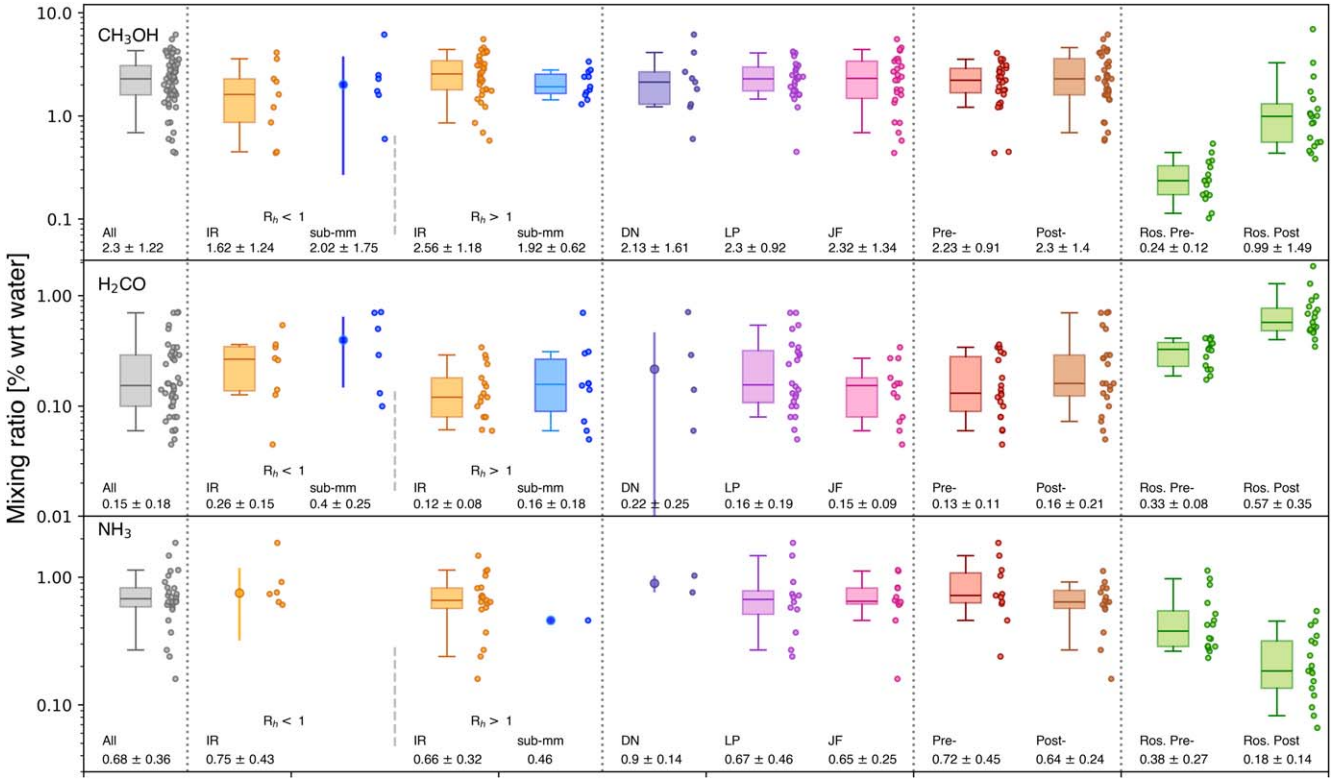

Figure 1. Box plot statistic for CH_3OH, H_2CO, and NH_3 abundances in comets. Starting from the left, we show the overall database, the heliocentric distance dependency ($R_h < 1$ vs. $R_h > 1$ au; see also Figure A1), different dynamical types (DN = dynamically new, LP = long-period, JF = Jupiter-family), pre- and post-perihelion observations, and 67P measurements separated in pre- and post-perihelion. For each box plot the middle line corresponds to the median, the box limits correspond to the 25th and 75th percentiles, and the whiskers correspond to the 5th and 95th percentiles. Below every box, we report the median ± standard deviation.

Table 1
Statistic of Mixing Ratios with Respect to Water for Methanol, Formaldehyde, and Ammonia, Considering the Different Samples Extracted from the Comet Molecular Database

	CH_3OH	H_2CO	NH_3	CH_3OH/H_2CO	NH_3/CH_3OH
All	2.30 ± 1.14 (60)	0.15 ± 0.14 (39)	0.68 ± 0.36 (26)	13.4 ± 14.6 (38)	0.28 ± 0.24 (26)
IR $R_h < 1$	1.62 ± 1.24 (9)	0.27 ± 0.15 (8)	0.75 ± 0.43 (6)	4.6 ± 6.4 (12)[a]	0.50 ± 0.34 (6)[a]
IR $R_h \geqslant 1$	2.56 ± 1.18 (36)	0.12 ± 0.08 (17)	0.66 ± 0.32 (19)	19.9 ± 14.7 (26)[a]	0.27 ± 0.16 (20)[a]
(Sub)millimeter $R_h < 1$	1.74 ± 0.66 (5)	0.29 ± 0.23 (5)	…	…	…
(Sub)millimeter $R_h \geqslant 1$	2.16 ± 0.63 (10)	0.15 ± 0.09 (9)	0.46 ± 0.04 (1)	…	…
Dynamically new	1.98 ± 1.01 (8)	0.14 ± 0.10 (3)	0.90 ± 0.14 (2)	9.3 ± 7.6 (3)	0.33 ± 0.15 (2)
Long-period	2.35 ± 0.92 (26)	0.15 ± 0.17 (23)	0.67 ± 0.46 (12)	13.4 ± 15.4 (22)	0.36 ± 0.29 (11)
Jupiter-family	2.32 ± 1.34 (26)	0.15 ± 0.09 (13)	0.65 ± 0.25 (12)	17.6 ± 13.9 (13)	0.26 ± 0.16 (11)
Pre-perihelion	2.23 ± 0.91 (27)	0.13 ± 0.11 (19)	0.72 ± 0.45 (11)	12.3 ± 10.3 (19)	0.38 ± 0.28 (10)
Post-perihelion	2.30 ± 1.29 (33)	0.16 ± 0.17 (20)	0.64 ± 0.24 (15)	15.0 ± 17.6 (19)	0.22 ± 0.19 (15)
Ros. pre-per	0.24 ± 0.12 (16)	0.33 ± 0.08 (16)	0.38 ± 0.27 (16)	1.25 ± 5.2 (16)	2.83 ± 2.07 (15)
Ros. post-per	0.99 ± 1.49 (19)	0.57 ± 0.35 (19)	0.18 ± 0.14 (17)	1.91 ± 0.88 (19)	0.20 ± 0.55 (17)

Notes. For each subset and for the CH_3OH/H_2CO and NH_3/CH_3OH ratios, we report the median ± standard deviation, with the sample size given in parentheses.
[a] IR and (sub)millimeter data are combined.

4. Planet-forming Systems

Molecular emission from the warm circumstellar regions around Class 0 protostars of 10^4 yr associated with hot corinos, as well as from disks around Class I (10^5 yr) and Class II ($\geqslant 10^6$ yr) sources, is observed at (sub)millimeter wavelengths through their lowest rotational transitions. In particular, formaldehyde is routinely detected and resolved in disks (e.g., Pegues et al. 2020; Garufi et al. 2021; Öberg et al. 2021), while methanol emission has proven harder to detect. According to disk models, CH_3OH can reach gas-phase abundances, $[CH_3OH]/[H_2]$, of up to 10^{-8} (e.g., Walsh et al. 2014), but due to its large partition function, the lines are fainter. Therefore, methanol has only been detected in a few disks to date: the Class 0 disk HH 212 (Lee et al. 2022); the

Table 2
Molecular Column Densities N_X in cm^{-2}, and Abundance Ratios in a Star-forming Cloud, in Hot Corinos around Class 0 Protostars and in Class I and II Planet-forming Disks

Source	N_{CH_3OH} (cm^{-2})	N_{H_2CO} (cm^{-2})	N_{NH_3} (cm^{-2})	$[CH_3OH]/[H_2CO]$	$[NH_3]/[CH_3OH]$	Reference
			Star-forming Cloud			
Cha MMS1 ($A_V \sim 60$)	$0.61^{+0.95}_{-0.28} \times 10^{18}$	⋯	$0.30^{+0.97}_{-0.21} \times 10^{18}$	⋯	$0.5^{+2.9}_{-0.3}$	(1)
Cha MMS1 ($A_V \sim 95$)	$0.51^{+1.08}_{-0.24} \times 10^{18}$	⋯	$0.66^{+1.11}_{-0.48} \times 10^{18}$	⋯	$1.3^{+3.3}_{-0.9}$	(1)
			Class 0 Hot Corinos and Disks			
IRAS2A	$5.0^{+2.9}_{-1.8} \times 10^{18}$	4.3×10^{17}	⋯	12^{+6}_{-5}	⋯	(2)
IRAS4A2	$1.6^{+0.6}_{-0.8} \times 10^{19}$	7.5×10^{17}	$0.6 - 3 \times 10^{18}$	21^{+8}_{-10}	0.015 − 0.5	(2), (3)
IRAS4B	$1–8 \times 10^{19}$	⋯	$0.2 - 3 \times 10^{18}$	⋯	0.003–0.3	(2), (3)
IRAS 16293–2422 B	2.3×10^{19}	$1.3^{+0.1}_{-0.1} \times 10^{18}$	⋯	18 ± 1	⋯	(4), (5)
IRAS 16293–2422 A	$1.3^{+0.4}_{-0.4} \times 10^{19}$	$1.2^{+0.5}_{-0.5} \times 10^{17}$	⋯	108 ± 56	⋯	(6)
HH 212 disk	$1.5^{+4.5}_{-0.8} \times 10^{18}$	$6.1^{+2.3}_{-2.3} \times 10^{16}$	⋯	25^{+132}_{-17}	⋯	(7)
			Class I Disks			
IRAS 04302	$(3.6 - 14.6) \times 10^{13}$	$(7.2 - 25) \times 10^{13}$	⋯	0.5 − 0.6	⋯	(8)
			Class II Disks			
TW Hya	$(4.7 - 13) \times 10^{12}$	$(3.7 - 7.5) \times 10^{12}$	$(0.8 - 13) \times 10^{12}$	1.3 − 1.7	0.06 − 2.7	(9), (10), (11)
HD 100546	$7.1^{+0.7}_{-0.6} \times 10^{12}$	$4.5^{+0.5}_{-0.5} \times 10^{12}$	⋯	1.6 ± 0.2	⋯	(12)
			Class II—Inner Disks, Dust Trap			
HD 100546 (20–50 au)	$1.5 \pm 0.3 \times 10^{14}$	$1.2 \pm 0.2 \times 10^{13}$	⋯	12.5 ± 2.5	⋯	(12)
HD 169142 (10–25 au)	$5 - 4 \times 10^{14}$	$4 - 6 \times 10^{12}$	⋯	120 − 60	⋯	(13)
Oph IRS 48 (dust trap)	$4.9 \pm 0.2 \times 10^{14}$	$7.7 \pm 0.5 \times 10^{13}$	⋯	6.4 ± 0.7	⋯	(14)

References. (1) McClure et al. 2023; (2) Taquet et al. 2015; (3) De Simone et al. 2022; (4) Jørgensen et al. 2016; (5) Persson et al. 2018; (6) Manigand et al. 2020; (7) Lee et al. 2022; (8) Podio et al. 2020; (9) Walsh et al. 2016; (10) Carney et al. 2019; (11) Salinas et al. 2016; (12) Booth et al. 2021; (13) Booth et al. 2023; (14) van der Marel et al. 2021.

Class I disk IRAS 04302+2247 (hereafter IRAS 04302; Podio et al. 2020); the Class II disk TW Hya (Walsh et al. 2016); the disks of the Herbig stars Oph IRS 48, HD 100547, and HD 169142 (Booth et al. 2021, 2023; van der Marel et al. 2021); and the disk around the young outbursting star V883 Ori (van't Hoff et al. 2018; Lee et al. 2019b). We build on these pioneer studies that first estimated the $[CH_3OH]/[H_2CO]$ in planet-forming disks, and we also add the $[CH_3OH]/[H_2CO]$ abundance ratios estimated in hot corinos around Class 0 protostars. We only consider hot corinos observed with interferometers, to avoid problems of beam dilution, namely, IRAS2A, IRAS4A2, and IRAS4B in the NGC 1333 cloud in Perseus (Taquet et al. 2015); the prototypical hot corino IRAS 16293–2422 B; and its close companion IRAS 16293-2422 A covered by the PILS spectral survey (Jørgensen et al. 2016; Persson et al. 2018; Manigand et al. 2020).

The transitions of ammonia can be detected in the far-IR or in the centimeter. There are only three detections of NH_3 emission lines available in the literature: for the bright Class II disk TW Hya, obtained with the Herschel space telescope and a beam of about 40″ (Salinas et al. 2016), and for the hot corinos IRAS4A2 and IRAS4B, obtained with the Karl G. Jansky Very Large Array (JVLA) interferometer (De Simone et al. 2022; Yamato et al. 2022). In addition, the JWST recently delivered estimates of molecular abundances in ices, including NH_3 and CH_3OH, toward two positions just outside the infalling envelope of the Class 0 protostar Cha MMS1 (McClure et al. 2023).

The CH_3OH, H_2CO, and NH_3 column densities and the $[CH_3OH]/[H_2CO]$ and $[NH_3]/[CH_3OH]$ abundance ratios in a star-forming cloud, in the Class 0 hot corinos, and in the Class 0, I, and II planet-forming disks are reported in Table 2, with the relative references. The procedure and assumptions adopted to derive the column densities for each individual source are summarized in Appendix C. For disks, we report both disk-averaged values of the column density and abundance ratios, and when radial profiles of the intensity and column density are available, we also report the values estimated in the inner disk region ($r < 25$–50 au), where the sublimation of ices releases all methanol and formaldehyde in gas phase (Booth et al. 2021; van der Marel et al. 2021; Booth et al. 2023). The estimated molecular abundance ratios are compared with the cometary values in Figure 2.

5. Discussion: Inheritance or Reset Scenario?

Assuming that the solar system formed in a similar way to other Sun-like stars, we examined the $[CH_3OH]/[H_2CO]$ and $[NH_3]/[CH_3OH]$ abundance ratios estimated in different planet-forming systems and in comets. The comparison is aimed to determine whether there are differences between planet-forming systems at the early stages of their formation and whether there are changes in molecular abundance ratios from the protostellar phase to planetesimal formation, providing hints on the chemical history of material during planet formation.

The $[CH_3OH]/[H_2CO]$ ratio in comets ranges between about 2 and 56. It is interesting to notice that the slight heliocentric dependency we have identified for the formaldehyde and methanol mixing ratios (Section 3.2) is much amplified when considering $[CH_3OH]/[H_2CO]$ abundances ratios, resulting in a median value of the ratio of 4.5 for comets at heliocentric distances <1 au and 25.5 for comets observed at >1 au from the Sun (see Tables 1 and B1 and Figures 2 and A2). Even if

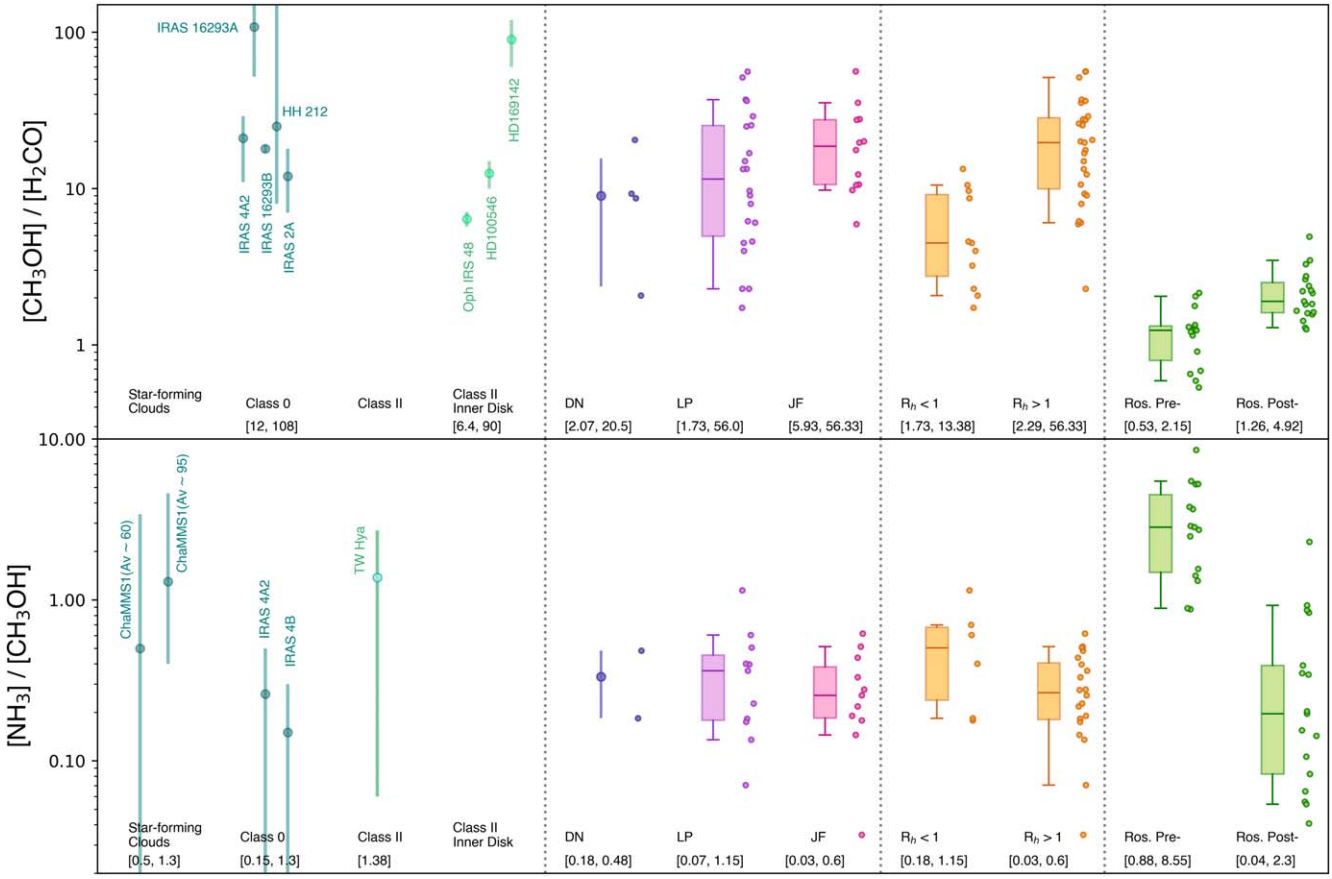

Figure 2. Box plot statistic for $[CH_3OH]/[H_2CO]$ and $[NH_3]/[CH_3OH]$ ratios in comets and comparison with disks. Below each box, the [minimum, maximum] interval values are indicated. Starting from the left, we show the ratios measured in planet-forming systems as listed in Table 2, in comets divided in different dynamical families (DN = dynamically new, LP = long-period, JF = Jupiter-family), in comets at different heliocentric distances ($R_h < 1$ vs. $R_h > 1$ au, see also Figure A2), and in 67P divided in pre- and post-perihelion. Below every box, we report the [min,max] intervals.

the number of comets observed within 1 au from the Sun is low compared to those observed at larger heliocentric distances (7 and 26 comets, respectively), the influence of this subgroup on the overall median is important and needs to be taken into account when comparing disks and comets. In fact, if the H_2CO mixing ratio is enhanced by secondary species produced in the coma in specific temperature conditions for comets observed at <1 au, then the estimated $[CH_3OH]/[H_2CO]$ ratio will be lower and not predictive of the real ice composition. It is worth mentioning also that the abundance ratios estimated in disks may not reflect the ice composition depending on the disk region where the line emission is integrated. In fact, the disk-averaged $[CH_3OH]/[H_2CO]$ abundance ratios are significantly lower than those measured in the inner disk (up to 50 au). As discussed in Booth et al. (2021), this may be due to the fact that the disk-integrated abundance ratios are more representative of the cold outer disk, where the dust temperature is low. In the outer disk CH_3OH cannot be thermally desorbed and only a tiny fraction of the ices is released in gas phase, due to nonthermal processes. On the other hand, H_2CO is abundantly formed in gas phase in the disk molecular layer out to large disk radii (e.g., Podio et al. 2020). Hence, the disk-averaged $[CH_3OH]/[H_2CO]$ abundance ratios are likely not predictive of the ice composition in the disk. Conversely, in the inner 50 au region of transition disks around Herbig stars all the ices are thermally sublimated; hence, the $[CH_3OH]/[H_2CO]$ abundance ratios are a good probe of the ice composition.

If we take this information into account, the methanol-to-formaldehyde abundance ratio retrieved considering only comets observed at heliocentric distances larger than 1 au ranges from about 6 to 56 (median value ≈25.5) and is compatible with the one observed in Class 0 objects, ranging from 12 to 108 (median value ≈21), and the ratio inferred in the inner regions of Class II disks, ranging from 6.4 to 120 (median value ≈12.5), as shown in Figure 2. Therefore, the comparison in Figure 2 indicates that the $[CH_3OH]/[H_2CO]$ ratio is similar in different planetary systems and remained constant across time (in star-forming clouds, in protostellar sources of 10^4 yr, and in disks of a few Myr), in the region of the disk where comets formed (≈10–50 au from the proto-Sun; e.g., Gomes et al. 2005). Since we do not see substantial differences between comets' dynamical classes, the $[CH_3OH]/[H_2CO]$ ratio is most likely preserved also during a comet's lifetime. It may be possible that a fraction of the interstellar medium (ISM) ices enclosed in refractory grains in the prestellar phase were kept insulated from heat and radiation (e.g., by residing in shadowed pockets, or shielded by the high dust content in the disk midplane) until being incorporated into the early planetesimals, and then in comets. The inheritance scenario is also supported by the comparison of the ammonia-to-methanol abundance ratios shown in the bottom panel of Figure 2. In comets, $[NH_3]/[CH_3OH]$ ranges approximately between 0.03 and 1.1 and is consistent with Class 0 and Class II sources (both displaying values lower than 2.7).

Unfortunately, in this case the samples are much smaller, especially considering planet-forming systems.

Finally, it is interesting to notice that data for 67P (Läuter et al. 2020; Biver et al. 2023; Bonev et al. 2023) may lead to a slightly different conclusion if used alone. In fact, 67P shows a lower range for the $[CH_3OH]/[H_2CO]$ ratio, with values ranging from 0.5 to 13.4. This may indicate that the material incorporated in the nucleus of this comet has a different formation history. Since 67P belongs to the JF comets, changes of its initial composition due to several Sun revolutions after formation are also possible. The average $[NH_3]/[CH_3OH]$ ratio of 0.2 retrieved for 67P post-perihelion observations is consistent with the overall comet database, while the pre-perihelion ratio of 2.86 is much higher and may again lead to a completely different interpretation. The examples of 67P and comets observed within 1 au from the Sun demonstrate that it is necessary to be cautious when comparing comets and disks and that the use of a single object or even a single measure may be not representative or exhaustive to reconstruct the planet formation chemical history. A statistical approach is more suitable, helping to investigate the diverse aspects of the chemistry of comets and planet-forming systems and the extent of material processing during the various stages of the solar system formation.

6. Conclusions

In this work, we implemented the first statistical comparison of the abundances of methanol, formaldehyde, and ammonia and their ratios in a sample of 35 comets and 11 planet-forming systems, i.e., young Sun-like stars with ages ranging from 10^4 yr (Class 0 sources) to 10^5–10^7 yr (Class I and II sources).

For comets, we provided mixing ratios with respect to water for these three species and their medians and standard deviations, considering ground-based IR and (sub)millimeter spectroscopy measurements. Given the sample's diversity, our statistics account for dynamical families, nuclei heterogeneity, and short- and long-term fluctuation, offering a comprehensive view of comet composition. We analyzed separately diverse subgroups (e.g., dynamical types, IR vs. (sub)millimeter) to search for observational and/or modeling biases. Additionally, we compared our database with the data collected for comet 67P as observed by the Rosina mass spectrometer on board Rosetta (Läuter et al. 2020).

IR and (sub)millimeter abundances are in agreement, both revealing an abundance ratio of $[CH_3OH]/[H_2CO]$ significantly higher for comets observed within 1 au from the Sun; further research on comets at heliocentric distances smaller than 1 au is required to investigate this difference, most likely due to temperature-activated processes in the coma. On the other hand, the Rosina-Rosetta measurements for 67P show different molecular abundances ratios compared to the overall database, as well as large discrepancies between pre- and post-perihelion estimates. This highlights the importance of our statistical approach: in fact, 67P abundances are often employed as the major and only reference when comparing planet-forming systems and comets (e.g., Bianchi et al. 2019; Drozdovskaya et al. 2019), introducing significant interpretation biases. A broader analysis is required to better understand these disparities.

The $[CH_3OH]/[H_2CO]$ and $[NH_3]/[CH_3OH]$ abundance ratios in the examined Class 0 protostars and in the inner regions of Class II disks, where the line emission is dominated by ice sublimation, are similar and consistent with those measured in the star-forming cloud probed by JWST and in comets. This supports statistically for the first time that (1) planet-forming systems share a similar chemistry and (2) the chemical complexity of comets may have been inherited already since the early phases of the formation of the solar system.

Our findings also highlight the need to further increase the statistic in both planet-forming systems and comets, especially for assessing undersampled molecular abundances such as ammonia in Class I objects and Oort Cloud comets.

Acknowledgments

We are sincerely grateful to Dr. G. P. Tozzi for the inspiring conversations that greatly improved our work.

This work is financially supported by the "NextGenerationEU" program, in the context of the "Piano Nazionale di Ripresa e Resilienza (PNRR)," project code SOE_0000188 ("ProDisCo—a systematic comparison between measured molecular abundances in comets and protoplanetary disks"; PI: Manuela Lippi). Cl.Co. and L.P. acknowledge the PRIN-MUR 2020 BEYOND-2p (Astrochemistry beyond the second period elements, Prot. 2020AFB3FX), the project ASI-Astrobiologia 2023 MIGLIORA (Modeling Chemical Complexity, F83C23000800005), the INAF-GO 2023 funding PROTO-SKA (Exploiting ALMA data to study planet-forming disks: preparing the advent of SKA, C13C23000770005), and the INAF Mini-Grant 2022 "Chemical Origins" (PI: L. Podio). L.P. and Cl.Co. acknowledge financial support under the National Recovery and Resilience Plan (NRRP), Mission 4, Component 2, Investment 1.1, Call for tender No. 104 published on 2.2.2022 by the Italian Ministry of University and Research (MUR), funded by the European Union —NextGenerationEU—Project Title 2022JC2Y93 Chemical Origins: linking the fossil composition of the Solar System with the chemistry of protoplanetary disks—CUP J53D23001600006 —Grant Assignment Decree No. 962 adopted on 30.06.2023 by the Italian Ministry of Ministry of University and Research (MUR). S. F., G. V., and M. M. acknowledge support from the NASA's Center for Astrobiology (GCA), Goddard's Fundamental Laboratory Research (FLaRe), and the Sellers Exoplanet Environments Collaboration (SEEC).

Software: Astropy (Price-Whelan et al. 2018), Matplotlib (Hunter 2007), Scipy (Virtanen et al. 2020), Numpy (Harris et al. 2020).

Appendix A
Comet Data

In Table A1 we report the data for each comet that we used for the presented statistics and results. For each comet we give each measurement of CH_3OH, H_2CO, NH_3, and the ratios of $[CH_3OH]/[H_2CO]$ and $[NH_3]/[CH_3OH]$ that we calculated for comparisons with planet-forming systems. For each comet the relative references are also provided. In Figures A1 and A2 we show the heliocentric dependency for each analyzed molecular species and their ratios, respectively.

Table A1
Methanol, Formaldehyde, and Ammonia Molecular Abundances in Comets and Relative References

Comet	Type	R_h[a]	CH_3OH	H_2CO	NH_3	$[CH_3OH]/[H_2CO]$	$[NH_3]/[CH_3OH]$	SR	Reference
2P/Encke	ET	−1.19	3.56 ± 0.27	<0.11	<0.7	⋯	⋯	IR	(1)
	ET	0.46	0.87 ± 0.09	0.27 ± 0.04	0.61 ± 0.04	3.22 ± 0.81	0.70 ± 0.12	IR	(6)
8P/Tuttle	HT	−1.16	2.61 ± 0.13	0.1 ± 0.02	0.72 ± 0.38	26.10 ± 6.52	0.28 ± 0.16	IR	(1)
9P/Tempel 1	JF	−1.52	2.22 ± 0.19	0.18 ± 0.07	1.14 ± 0.72	12.33 ± 5.85	0.51 ± 0.37	IR	(1)
10P/Tempel 2	JF	1.44	1.81 ± 0.21	<0.135	1.12 ± 0.24	⋯	0.62 ± 0.20	IR	(1)
17P/Holmes	JF	2.455	4.3 ± 0.43	<0.24	0.82 ± 0.52	⋯	0.19 ± 0.14	IR	(1)
21P /Giacobini	JF	−1.172	2.87 ± 0.94	⋯	<2.75	⋯	⋯	IR	(3)
-Zinner	JF	−1.12	3.41 ± 0.62	<0.15	<2.97	⋯	⋯	IR	(3)
	JF	−1.013	1.35 ± 0.17	<0.05	<0.48	⋯	⋯	IR	(3)
	JF	1.08	0.69 ± 0.29	<0.05	⋯	⋯	⋯	IR	(3)
	JF	1.04	1.7 ± 0.1	0.16 ± 0.02	⋯	10.63 ± 1.95	⋯	(sub)mm	(4)
45P/Honda-Mrkos	JF	−0.55	3.59 ± 0.31	0.34 ± 0.08	0.64 ± 0.24	10.56 ± 3.40	0.18 ± 0.08	IR	(7)
-Pajdušáková	JF	1.01	4.6 ± 0.76	0.13 ± 0.03	0.16 ± 0.06	35.39 ± 14.01	0.04 ± 0.02	IR	(8)
	JF	1.099	4.41 ± 0.77	0.16 ± 0.05	0.64 ± 0.14	27.56 ± 13.43	0.15 ± 0.06	IR	(8)
46P/Wirtanen	JF	1.057	3.03 ± 0.23	<0.064	0.66 ± 0.029	⋯	0.22 ± 0.03	IR	(9)
	JF	−1.07	2.7 ± 0.1	0.153 ± 0.031	⋯	17.65 ± 4.23	⋯	(sub)mm	(10)
	JF	1.06	3.38 ± 0.03	0.06 ± 0.01	⋯	56.33 ± 9.89	⋯	(sub)mm	(11)
67P/Churyumov-	JF	1.22	1.44 ± 0.07	0.073 ± 0.01	⋯	19.73 ± 3.66	⋯	(sub)mm	(12)
Gerasimenko	JF	1.255	0.58 ± 0.10	<0.08	<0.55	⋯	⋯	IR	(13)
	JF	1.331	0.86 ± 0.14	<0.05	<0.27	⋯	⋯	IR	(13)
73P/Schwassman-Wachmann[b]	JF	−1.0	0.44 ± 0.03	0.045 ± 0.005	<0.23	9.78 ± 1.75	⋯	IR	(1)
81P/Wild 2	JF	1.598	1.6 ± 0.4	0.27 ± 0.09	0.7 ± 0.3	5.93 ± 3.46	0.44 ± 0.30	IR	(14)
103P/Hartley 2	JF	−1.203	2.41 ± 0.33	0.12 ± 0.06	<1.53	20.08 ± 12.79	⋯	IR	(1)
	JF	−1.069	2.23 ± 0.06	0.08 ± 0.02	0.62 ± 0.17	27.88 ± 7.72	0.28 ± 0.08	IR	(1)
	JF	1.064	2.51 ± 0.09	<0.02	0.83 ± 0.14	⋯	0.33 ± 0.07	IR	(1)
153P/Ikeya-Zhang	LP	1.0	2.5 ± 0.10	0.1 ± 0.01	⋯	25.0 ± 3.5	⋯	(sub)mm	(2)
252P/LINEAR	JF	1.17	5.56 ± 0.66	<0.18	<0.77	⋯	⋯	IR	(5)
C/1999 H1 (Lee)	LP	1.05	3.20 ± 0.16	0.24 ± 0.04	0.56 ± 0.15	13.33 ± 2.89	0.18 ± 0.06	IR	(1)
C/1999 T1	LP	1.28	4.22 ± 0.69	<0.3	<6.3	⋯	⋯	IR	(1)
(McNaught-Hartley)	LP	1.3	2.4 ± 0.3	0.16 ± 0.04	⋯	15.00 ± 5.63	⋯	(sub)mm	(2)
C/2000 WM1	DN	−1.34	1.23 ± 0.08	0.06 ± 0.02	<0.63	20.51 ± 8.17	⋯	IR	(1)
(LINEAR)	DN	−1.2	1.3 ± 0.2	0.14 ± 0.05	⋯	9.29 ± 4.75	⋯	(sub)mm	(2)
C/2001 A2 (LINEAR)	LP	1.165	4.11 ± 0.25	0.08 ± 0.02	<0.51	51.38 ± 15.97	0.124 ± 0.008	IR	(1)
	LP	1.1	2.8 ± 0.4	0.05 ± 0.01	⋯	56.00 ± 19.20	⋯	(sub)mm	(2)
C/2001 Q4 (NEAT)	LP	−0.97	1.74 ± 0.28	0.13 ± 0.03	⋯	13.39 ± 5.24	⋯	(sub)mm	(15)
C/2003 K4 (LINEAR)	DN	1.28	1.83 ± 0.16	<0.07	<0.0	⋯	-	IR	(16)
C/2004 Q2 (Machholz)	LP	−1.485	4.08 ± 0.39	0.11 ± 0.05	<1.3	37.09 ± 20.41	⋯	IR	(1)
	LP	−1.21	1.77 ± 0.06	0.061 ± 0.008	0.24 ± 0.01	29.02 ± 4.79	0.14 ± 0.01	IR	(1)
C/2006 P1 (McNaught)	DN	0.23	0.6 ± 0.2	0.29 ± 0.06	⋯	2.07 ± 1.12	⋯	(sub)mm	(17)
C/2007 N3 (Lulin)	LP	1.26	3.82 ± 0.15	0.15 ± 0.02	0.27 ± 0.16	25.47 ± 4.40	0.07 ± 0.05	IR	(1)
C/2007 W1 (Boattini)	DN	0.895	4.13 ± 0.29	<0.03	0.76 ± 0.14	⋯	0.18 ± 0.05	IR	(1)
C/2009 P1 (Garrad)	DN	−1.83	2.13 ± 0.46	<0.11	1.03 ± 0.81	⋯	0.48 ± 0.49	IR	(1)
	DN	1.57	2.32 ± 0.19	<0.08	<0.66	⋯	⋯	IR	(1)
C/2012 F6 (Lemmon)	LP	1.737	1.46 ± 0.2	<0.08	0.58 ± 0.23	⋯	0.40 ± 0.21	IR	(1)
C/2012 K1	DN	−1.84	2.69 ± 0.21	<0.14	<1.8	⋯	⋯	IR	(18)

Table A1
(Continued)

Comet	Type	R_h[a]	CH_3OH	H_2CO	NH_3	$[CH_3OH]/[H_2CO]$	$[NH_3]/[CH_3OH]$	SR	Reference
(PanSTARRS)									
C/2013 R1 (Lovejoy)	LP	−1.3	2.92 ± 0.2	0.08 ± 0.03	1.48 ± 0.28	36.50 ± 16.19	0.51 ± 0.13	IR	(1)
	LP	0.92	1.6 ± 0.2	0.7 ± 0.07	⋯	2.29 ± 0.51	⋯	(sub)mm	(19)
C/2013 V5 (Oukaimeden)	LP	−0.78	1.22 ± 0.04	0.126 ± 0.018	0.74 ± 0.08	9.68 ± 1.70	0.61 ± 0.09	IR	(20)
C/2014 Q2 (Lovejoy)	LP	1.29	1.76 ± 0.08	0.29 ± 0.03	0.64 ± 0.06	6.07 ± 0.90	0.36 ± 0.05	IR	(21)
	LP	−1.3	2.4 ± 0.5	0.3 ± 0.06	⋯	8.00 ± 3.27	⋯	(sub)mm	(22)
C/2015 ER_{61} (PanSTARRS)	LP	−1.11	3.08 ± 0.23	0.34 ± 0.07	0.7 ± 0.15	9.06 ± 2.54	0.23 ± 0.07	IR	(23)
	LP	1.04	2.02 ± 0.26	0.12 ± 0.03	0.37 ± 0.09	16.83 ± 6.38	0.18 ± 0.07	IR	(23)
	LP	−1.13	1.92 ± 0.73	0.31 ± 0.03	⋯	6.19 ± 2.95	⋯	(sub)mm	(24)
C/2017 E4 (Lovejoy)	LP	−0.66	1.62 ± 0.10	0.36 ± 0.03	1.86 ± 0.36	4.50 ± 0.65	1.15 ± 0.29	IR	(25)
C/2018 Y1 (Iwamoto)	LP	−1.287	3.10 ± 0.30	<0.069	<0.29	⋯	⋯	IR	(26)
C/2020 F3 (NEOWISE)	LP	0.92	2.29 ± 0.25	<0.14	0.92 ± 0.19	⋯	0.40 ± 0.13	IR	(27)
	LP	0.56	2.16 ± 0.14	0.54 ± 0.13	<1.15	4.00 ± 1.22	⋯	IR	(27)
	LP	0.7	2.3 ± 0.1	0.5 ± 0.2	⋯	4.60 ± 2.04	⋯	(sub)mm	(28)
C/2021 A1 (Leonard)	LP	0.62	<0.07	0.14 ± 0.01	<0.43	⋯	⋯	IR	(29)
	LP	−0.62	0.45 ± 0.03	0.26 ± 0.02	<0.6	1.73 ± 0.25	⋯	IR	(30)

Notes.
[a] Negative values indicate pre-perihelion measurements.
[b] For comet 73P/Schwassmann-Wachmann we merged molecular abundances retrieved from fragments B and C.

References: (1) Lippi et al. 2021; (2) Biver et al. 2006; (3) Faggi et al. 2019; (4) Biver et al. 2021b; (5) Paganini et al. 2019; (6) Roth et al. 2018; (7) DiSanti et al. 2017; (8) Dello Russo et al. 2020; (9) Bonev et al. 2021; (10) Cordiner et al. 2023; (11) Biver et al. 2021a; (12) Biver et al. 2023; (13) Bonev et al. 2023; (14) Dello Russo et al. 2016; (15) de Val-Borro et al. 2013; (16) Paganini et al. 2015; (17) Biver et al. 2011; (18) Roth et al. 2017; (19) Biver et al. 2014; (20) DiSanti et al. 2018; (21) Dello Russo et al. 2022; (22) Biver et al. 2015; (23) Saki et al. 2021; (24) Roth et al. 2021; (25) Faggi et al. 2018; (26) DiSanti et al. 2021; (27) Faggi et al. 2021; (28) Biver et al. 2022a; (29) Faggi et al. 2023; (30) Lippi et al. 2023.

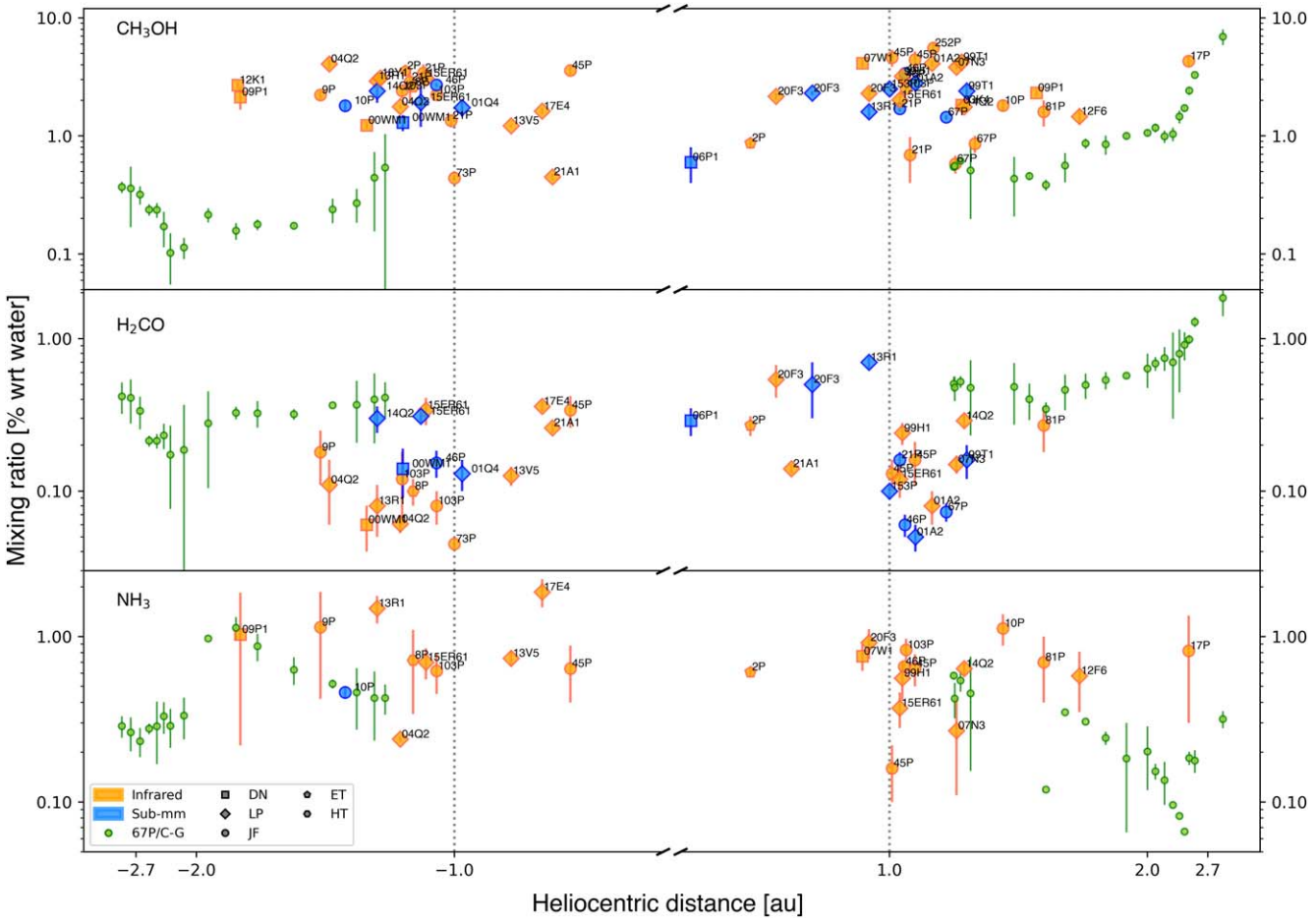

Figure A1. Mixing ratios with respect to water of CH_3OH, H_2CO, and NH_3 as a function of the heliocentric distance. Data from IR and (sub)millimeter observations are color-coded in yellow and blue, respectively, while 67P Rosetta mass spectrometer measurements are in green. Dynamical types are coded with symbols, with squares, diamonds, circles, pentagons, and hexagons representing DN, LP, JF, ET, and HT comets, respectively.

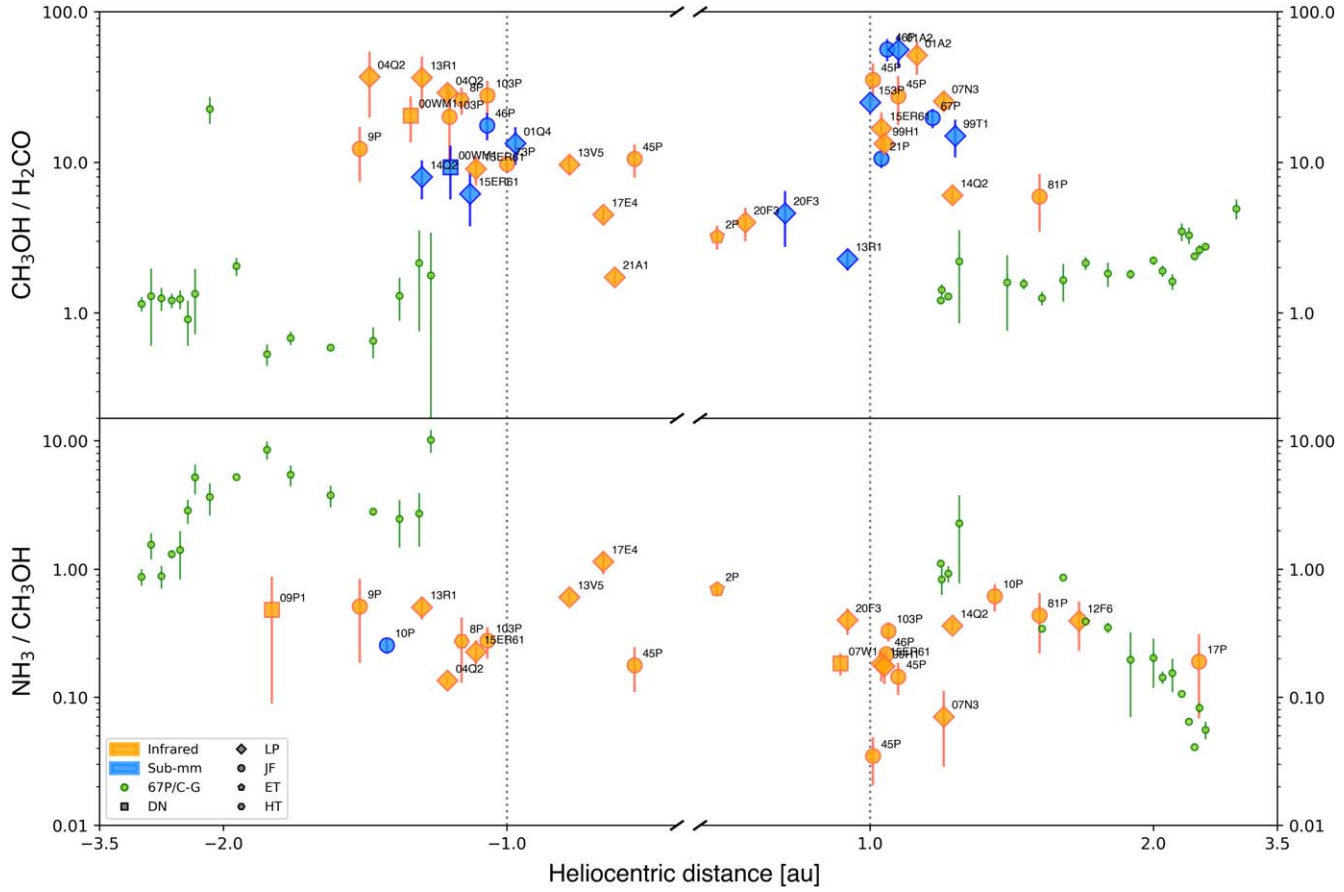

Figure A2. Heliocentric dependence of the $[CH_3OH]/[H_2CO]$ and $[NH_3]/[CH_3OH]$ ratios in comets. Data from IR and (sub)millimeter observations are color-coded in yellow and blue, respectively, while 67P Rosetta mass spectrometer measurements are in green. Dynamical types are coded with symbols, with squares, diamonds, circles, pentagons, and hexagons representing DN, LP, JF, ET, and HT comets, respectively.

Appendix B
Kolmogorov–Smirnov Test Applied to the Comet Database

The Kolmogorov–Smirnov test is a nonparametric test used to measure the shape of the sampling distributions. It is particularly useful for comparing two samples when the underneath distribution is not known. Here we report the results of this test applied to our subsamples of comet data. As a result of the test, a p-value <0.05 suggests a significant statistical difference between the two considered samples. In Table B1 we report the results of the Kolmogorov–Smirnov test applied to different Subsamples of comets.

Table B1
Kolomogrov–Smirnov Test Applied to Different Subsamples Extracted from the Comet Database

Sample 1	Sample 2	CH_3OH	H_2CO	NH_3	$[CH_3OH]/[H_2CO]$	$[NH_3]/[CH_3OH]$
DN	LP	0.56	0.91	0.22	0.75	0.99
DN	JF	0.56	0.99	0.33	0.45	0.99
JF	LP	0.73	0.47	0.87	0.36	0.99
$R_h > 1$	$R_h \leqslant 1$	0.10	0.08	0.45	$\mathbf{2.7 \times 10^{-3}}$	0.24
Pre-p.	Post-p.	0.44	0.82	0.52	0.54	0.32
Ros. pre-p.	Ros. post-p.	$\mathbf{2.9 \times 10^{-7}}$	$\mathbf{8.4 \times 10^{-8}}$	**0.002**	$\mathbf{6.5 \times 10^{-4}}$	$\mathbf{1.7 \times 10^{-6}}$
Pre-p.	Ros. pre-p.	$\mathbf{1.3 \times 10^{-9}}$	$\mathbf{0.8 \times 10^{-3}}$	**0.01**	$\mathbf{2.1 \times 10^{-7}}$	$\mathbf{4.1 \times 10^{-6}}$
Post-p.	Ros. post-p.	$\mathbf{2.2 \times 10^{-4}}$	$\mathbf{5.9 \times 10^{-8}}$	$\mathbf{1.8 \times 10^{-5}}$	$\mathbf{4.2 \times 10^{-6}}$	0.58

Note. p-values <0.05 are marked in bold.

Appendix C
Derivation of Abundance Ratios in Planet-forming Systems

As explained in Section 4, the abundance ratios $[CH_3OH]/[H_2CO]$ and $[NH_3]/[CH_3OH]$ in Class 0 hot corinos and in Class 0, I, and II disks are estimated through a radiative transfer analysis of the molecular transitions observed in the millimeter and centimeter ranges. In particular, the molecular column density (N_X in cm^{-2}) and the excitation temperature (T_{ex} in K) are derived from a rotational diagram (RD) analysis of the detected transitions by assuming optically thin emission and that the levels are populated in local thermodynamic equilibrium (LTE). When four or more transitions are observed, N_X and T_{ex} can be estimated by taking into account the line opacity through a population diagram (PD) analysis, which assumes LTE populations (e.g., Taquet et al. 2015), or through a radiative transfer model in large velocity gradient (LVG) approximation, which computes the level populations in non-LTE (e.g., De Simone et al. 2022). Optical depth effects on column density estimates are minimized when emission lines from molecular isotopologues are detected (e.g., $^{13}CH_3OH$, $CH_3^{18}OH$, $H_2^{13}CO$, $H_2C^{18}O$; e.g., Persson et al. 2018). When only one line is detected for a molecule, its column density is estimated by assuming LTE, optically thin emission at the temperature derived for one of the other species. Below, we detail the procedure adopted to derive the column densities and abundance ratios for each of the hot corinos and disks reported in Table 2. In addition, we briefly report on the derivation of the NH_3 and CH_3OH column densities in the ices, obtained from JWST observations of the IR absorption features toward the cloud of the Class 0 source Cha MMS1 (also reported in Table 2).

The Cloud of the Class 0 Source Cha MMS1.—The Class 0 protostar, Cha MMS1, is located in the low-mass star-forming region Chameleon I at 192 pc. The composition of the ices just outside the protostellar infalling envelope has been recently probed by JWST observations in the context of the Ice Age program (McClure et al. 2023). More precisely, the ice spectra are taken toward two background stars, NIR38 and SSTSL2 J110621.63−772354.1, which samples two lines of sight with visual extinction, $A_V \sim 60$ and $A_V \sim 95$, respectively.

The Class 0 Hot Corinos IRAS2A, IRAS4A2, IRAS4B2.—The IRAS2A, IRAS4A2, and IRAS4B protostellar sources are located in the Perseus star-forming region NGC 1333, at $d = 293$ pc, and are associated with bright hot corino emission (e.g., De Simone et al. 2017). The column densities of CH_3OH and H_2CO are estimated using observations taken with the IRAM Plateau de Bure Interferometer at $\sim 2''$ (i.e., 600 au) resolution, (Taquet et al. 2015). In particular, the column densities of CH_3OH are derived from the PD analysis of CH_3OH and $^{13}CH_3OH$ lines, while N_{H_2CO} is derived from $H_2^{13}CO$ assuming an isotopic ratio $^{12}C/^{13}C = 68$ and the same T_{ex} and source size as derived for CH_3OH ($T_{ex} = 140 \pm 20$ K, source size $0\farcs36 \pm 0\farcs04$ for IRAS2A; $T_{ex} = 140 \pm 30$ K, source size $0\farcs20^{+0\farcs08}_{-0\farcs04}$ for IRAS4A2). For IRAS4A2 and IRAS4B the column densities of CH_3OH and NH_3 are derived by De Simone et al. (2022) using Atacama Large Millimeter/submillimeter Array (ALMA) and JVLA data at $\sim 1''$, i.e., $\sim$300 au, from the simultaneous fitting of CH_3OH and NH_3 lines at millimeter and centimeter wavelengths using a non-LTE radiative transfer analysis. For IRAS4A2, they find a source size and T_{ex} for CH_3OH in agreement with those estimated by Taquet et al. (2015; $T_{ex} = 140$–160 K, source size $0\farcs19$–$0\farcs24$).

The Class 0 Hot Corinos IRAS 16293-2422 A and B.—The Class 0 binary system IRAS 16293–2422 consists of two sources, A and B, and is located in the L1689 region in the ρ Ophiuchus star-forming region at a distance of 120 pc (e.g., Jørgensen et al. 2016). IRAS 16293–2422 is the prototypical hot corino and has been observed with ALMA at $\sim 0\farcs5$, i.e., $\sim$60 au resolution by the PILS program (Jørgensen et al. 2016). Column densities are derived by Persson et al. (2018) and Manigand et al. (2020) from $CH_3^{18}OH$ and $H_2C^{18}O$ assuming a standard ISM $^{16}O/^{18}O$ ratio of 560 (Wilson & Rood 1994). For IRAS 16293 A, Manigand et al. (2020) estimated $T_{ex} = 130 \pm 26$ K for CH_3OH and $T_{ex} = 155 \pm 31$ K for H_2CO. For IRAS 16293 B, Jørgensen et al. (2018) and Persson et al. (2018) estimated $T_{ex} = 300$ K for CH_3OH and $T_{ex} = 106$ K for H_2CO.

The Class 0 Disk HH 212.—The disk/jet/hot corino protostellar system HH 212 is located in Orion at a distance of $\sim$400 pc (e.g., Codella et al. 2014). Lee et al. (2022) analyzed ALMA observations at $\sim 0\farcs05$, i.e., $\sim$20 au, to estimate molecular column densities in the disk. In particular, they estimated the column density of CH_3OH as the mean value of the estimates derived from two methods: (i) a non-LTE LVG analysis of the low-J rotational transitions ($E_{up} < 200$ K), and (ii) an RD, under the assumption of LTE, optically thin emission for the high-J rotational transitions ($E_{up} > 200$ K). The mean estimated temperature is $T_{ex} = 92^{+48}_{-37}$ K. The column density of H_2CO is derived from $H_2^{13}CO$, assuming $T_{ex} = 60 \pm 20$ K. The value published by Lee et al. (2022) is obtained assuming an isotopic ratio $^{12}C/^{13}C = 50$, while we here report the value obtained correcting for $^{12}C/^{13}C = 68$, for uniformity with the rest of the sources in the sample.

The Class I Disk IRAS 04302+2247.—The Class I source IRAS 04302+2247, also known as the butterfly star, is located in Taurus at $d \sim 161$ pc. The disk has been mapped at $0\farcs3$ resolution ($\sim$50 au) in several molecules, including H_2CO, while CH_3OH is detected only in the disk-integrated spectrum. Column densities are disk averaged and are derived assuming LTE, optically thin emission at $T_{ex} = 20$–100 K (Podio et al. 2020).

The Class II Disk TW Hya.—TW Hydrae (TW Hya) is a 0.6 $M_\odot$, 10 million year old T Tauri star at $\sim$54 pc distance. Due to its proximity, bright continuum, and presence of several molecular emission lines it is one of the most chemically characterized disks. The CH_3OH and H_2CO emissions have been mapped with ALMA at $\sim 1''$ ($\sim$50 au) and $\sim 0\farcs5$ ($\sim$25 au), respectively (Walsh et al. 2016; Öberg et al. 2017). The column densities of CH_3OH and H_2CO are disk averaged and derived assuming $T_{ex} = 25$–75 K (Carney et al. 2019). The CH_3OH column density is derived from the stacked map by Walsh et al. (2016). The NH_3 mass is estimated from Salinas et al. (2016) based on Herschel/HIFI observations (beam of $\sim 36''$) and converted into a column density assuming a disk radius $R = 240$ au.

The Herbig Ae/Be Disk HD 100546.—HD 100546 is an intermediate-aged ($\sim$5 Myr) Herbig Be star ($\sim$2.2 $M_\odot$) at a distance of $\sim$110 pc, surrounded by a warm and gas-rich disk (e.g., Booth et al. 2021). In Table 2 we report both the disk-averaged column densities and their mean values in the inner 20–50 au disk region as estimated by Booth et al. (2021), from the analysis of ALMA observations at $\sim 1\farcs2$ ($\sim$130 au). The disk-averaged column densities are derived from disk-

integrated line intensities assuming LTE, optically thin emission at $T_{ex} = 34 \pm 2$ K, which is inferred from the RD of H_2CO lines. Column densities and temperature profiles of H_2CO are then derived from the RD analysis applied at each radius of the line emission profiles. The column density profile of CH_3OH is obtained assuming the same T_{ex} as derived for H_2CO. We take average values of N_X in the inner 50 au, where $T_{ex} \sim 75 \pm 25$ K.

The Herbig Ae/Be Disk HD 169142.—HD 169142 is a nearby (∼114 pc) F1 star hosting an almost face-on gas-rich protoplanetary disk. Line emission in the disk was observed by several ALMA programs at resolution varying between ∼0.″17 (i.e., ∼20 au) and ∼0.″6 (i.e., 68 au). Column densities and temperature radial profiles of H_2CO and CH_3OH are derived from the line emission profiles assuming LTE at $T_{ex} = 60$ K. We report the range of values at $r \sim 10$–25 au estimated by Booth et al. (2023).

The Herbig Ae/Be Disk Oph IRS 48.—Oph IRS 48 is an A0 star located in the Ophiuchus cloud at a distance of ∼135 pc, with a large dust trap, where emission from CH_3OH and H_2CO is observed with ALMA at ∼0.″56 (i.e., ∼76 au) resolution (van der Marel et al. 2021). The molecular column densities and temperature are derived from H_2CO and CH_3OH RDs, finding $T_{ex} = 173^{+11}_{-9}$ K for H_2CO and $T_{ex} = 103^{+6}_{-5}$ K for CH_3OH and the N values reported in Table 2 (van der Marel et al. 2021).

ORCID iDs

Manuela Lippi https://orcid.org/0000-0001-9185-878X
Linda Podio https://orcid.org/0000-0003-2733-5372
Claudio Codella https://orcid.org/0000-0003-1514-3074
Sara Faggi https://orcid.org/0000-0003-0194-5615
Marta De Simone https://orcid.org/0000-0001-5659-0140
Geronimo L. Villanueva https://orcid.org/0000-0002-2662-5776
Michael J. Mumma https://orcid.org/0000-0003-4627-750X
Cecilia Ceccarelli https://orcid.org/0000-0001-9664-6292

References

Bianchi, E., Codella, C., Ceccarelli, C., et al. 2019, MNRAS, 483, 1850
Biver, N., Bockelée-Morvan, D., Boissier, J., et al. 2021a, A&A, 648, A49
Biver, N., Bockelée-Morvan, D., Colom, P., et al. 2011, A&A, 528, A142
Biver, N., Bockelée-Morvan, D., Crovisier, J., et al. 2006, A&A, 449, 1255
Biver, N., Bockelée-Morvan, D., Crovisier, J., et al. 2023, A&A, 672, A170
Biver, N., Bockelée-Morvan, D., Debout, V., et al. 2014, A&A, 566, L5
Biver, N., Bockelée-Morvan, D., Lis, D. C., et al. 2021b, A&A, 651, A25
Biver, N., Bockelée-Morvan, D., Moreno, R., et al. 2015, SciA, 1, 1500863
Biver, N., Boissier, J., Bockelée-Morvan, D., et al. 2022a, A&A, 668, A171
Biver, N., Crovisier, J., Bockelée-Morvan, D., et al. 2012, A&A, 539, A68
Biver, N., Dello Russo, N., Opitom, C., & Rubin, M. 2022b, arXiv:2207.04800
Bockelée-Morvan, D., & Biver, N. 2017, RSPTA, 375, 20160252
Bockelée-Morvan, D., Crovisier, J., Mumma, M. J., & Weaver, H. A. 2004, in Comets II, ed. M. C. Festou, H. U. Keller, & H. A. Weaver (Tucson, AZ: Univ. of Arizona Press), 391
Bonev, B. P. 2005, PhD thesis, Univ.of Toledo, Ohio
Bonev, B. P., Dello Russo, N., DiSanti, M. A., et al. 2021, PSJ, 2, 45
Bonev, B. P., Dello Russo, N., Kawakita, H., et al. 2023, AJ, 166, 233
Boogert, A. C. A., Gerakines, P. A., & Whittet, D. C. B. 2015, ARA&A, 53, 541
Booth, A. S., Law, C. J., Temmink, M., Leemker, M., & Macías, E. 2023, A&A, 678, A146
Booth, A. S., Walsh, C., Terwisscha van Scheltinga, J., et al. 2021, NatAs, 5, 684
Bottinelli, S., Boogert, A. C. A., Bouwman, J., et al. 2010, ApJ, 718, 1100
Brasser, R., & Morbidelli, A. 2013, Icar, 225, 40
Carney, M. T., Hogerheijde, M. R., Guzmán, V. V., et al. 2019, A&A, 623, A124
Ceccarelli, C. 2004, in ASP Conf. Ser. 323, Star Formation in the Interstellar Medium: In Honor of David Hollenbach, ed. D. Johnstone et al. (San Francisco, CA: ASP), 195
Ceccarelli, C., Caselli, P., Bockelée-Morvan, D., et al. 2014, in Protostars and Planets VI, ed. H. Beuther et al. (Tucson, AZ: Unive. of Arizona Press), 859
Ceccarelli, C., Caselli, P., Fontani, F., et al. 2017, ApJ, 850, 176
Ceccarelli, C., Codella, C., Balucani, N., et al. 2023, in ASP Conf. Ser. 534, Protostars and Planets VII, ed. S. Inutsuka et al. (San Francisco, CA: ASP), 379
Codella, C., Cabrit, S., Gueth, F., et al. 2014, A&A, 568, L5
Cordiner, M., Roth, N., Milam, S., et al. 2023, AAS/Division for Planetary Sciences Meeting Abstracts, 55, 400.02
De Simone, M., Ceccarelli, C., Codella, C., et al. 2022, ApJL, 935, L14
De Simone, M., Codella, C., Testi, L., et al. 2017, A&A, 599, A121
de Val-Borro, M., Küppers, M., Hartogh, P., et al. 2013, A&A, 559, A48
Dello Russo, N., Kawakita, H., Bonev, B. P., et al. 2020, Icar, 335, 113411
Dello Russo, N., Kawakita, H., Vervack, R. J., & Weaver, H. A. 2016, Icar, 278, 301
Dello Russo, N., Vervack, R. J., Kawakita, H., et al. 2022, PSJ, 3, 6
DiSanti, M. A., Bonev, B. P., Dello Russo, N., et al. 2021, PSJ, 2, 225
DiSanti, M. A., Bonev, B. P., Gibb, E. L., et al. 2018, AJ, 156, 258
DiSanti, M. A., Bonev, B. P., Russo, N. D., et al. 2017, AJ, 154, 246
Drozdovskaya, M. N., van Dishoeck, E. F., Rubin, M., Jørgensen, J. K., & Altwegg, K. 2019, MNRAS, 490, 50
Eistrup, C., Walsh, C., & van Dishoeck, E. F. 2018, A&A, 613, A14
Eistrup, C., Walsh, C., & van Dishoeck, E. F. 2019, A&A, 629, A84
Faggi, S., Lippi, M., Camarca, M., et al. 2021, AJ, 162, 178
Faggi, S., Lippi, M., Mumma, M. J., & Villanueva, G. L. 2023, PSJ, 4, 8
Faggi, S., Mumma, M. J., Villanueva, G. L., Paganini, L., & Lippi, M. 2019, AJ, 158, 254
Faggi, S., Villanueva, G. L., Mumma, M. J., & Paganini, L. 2018, AJ, 156, 68
Ferrero, S., Zamirri, L., Ceccarelli, C., et al. 2020, ApJ, 904, 11
Fray, N., Bénilan, Y., Biver, N., et al. 2006, Icar, 184, 239
Garufi, A., Podio, L., Codella, C., et al. 2021, A&A, 645, A145
Gomes, R., Levison, H. F., Tsiganis, K., & Morbidelli, A. 2005, Natur, 435, 466
Harris, C. R., Millman, K. J., van der Walt, S. J., et al. 2020, Natur, 585, 357
Haser, L. 1957, BSRSL, 43, 740
Herbst, E., & van Dishoeck, E. F. 2009, ARA&A, 47, 427
Hunter, J. D. 2007, CSE, 9, 90
Jonusas, M., Leroux, K., & Krim, L. 2020, JMoSt, 1220, 128736
Jørgensen, J. K., Müller, H. S. P., Calcutt, H., et al. 2018, A&A, 620, A170
Jørgensen, J. K., van der Wiel, M. H. D., Coutens, A., et al. 2016, A&A, 595, A117
Läuter, M., Kramer, T., Rubin, M., & Altwegg, K. 2020, MNRAS, 498, 3995
Le Roy, L., Altwegg, K., Balsiger, H., et al. 2015, A&A, 583, A1
Lee, C.-F., Codella, C., Ceccarelli, C., & López-Sepulcre, A. 2022, ApJ, 937, 10
Lee, C.-F., Codella, C., Li, Z.-Y., & Liu, S.-Y. 2019a, ApJ, 876, 63
Lee, J.-E., Lee, S., Baek, G., et al. 2019b, NatAs, 3, 314
Lippi, M. 2010, PhD thesis, Technical Univ. of Braunschweig, Germany
Lippi, M., Vander Donckt, M., Faggi, S., et al. 2023, A&A, 676, A105
Lippi, M., Villanueva, G. L., Mumma, M. J., & Faggi, S. 2021, AJ, 162, 74
Manigand, S., Jørgensen, J. K., Calcutt, H., et al. 2020, A&A, 635, A48
McClure, M. K., Rocha, W. R. M., Pontoppidan, K. M., et al. 2023, NatAs, 7, 431
Minissale, M., Aikawa, Y., Bergin, E., et al. 2022, ESC, 6, 597
Morbidelli, A., & Rickman, H. 2015, A&A, 583, A43
Mumma, M. J., & Charnley, S. B. 2011, ARA&A, 49, 471
Öberg, K. I., Guzmán, V. V., Merchantz, C. J., et al. 2017, ApJ, 839, 43
Öberg, K. I., Guzmán, V. V., Walsh, C., et al. 2021, ApJS, 257, 1
Paganini, L., Camarca, M. N., Mumma, M. J., et al. 2019, AJ, 158, 98
Paganini, L., Mumma, M. J., Villanueva, G. L., DiSanti, M. A., & Bonev, B. P. 2015, ApJ, 808, 1
Pegues, J., Öberg, K. I., Bergner, J. B., et al. 2020, ApJ, 890, 142
Persson, M. V., Jørgensen, J. K., Müller, H. S. P., et al. 2018, A&A, 610, A54
Podio, L., Garufi, A., Codella, C., et al. 2020, A&A, 642, L7
Price-Whelan, A. M., Sipőcz, B. M., Günther, H. M., et al. 2018, AJ, 156, 123
Rimola, A., Taquet, V., Ugliengo, P., Balucani, N., & Ceccarelli, C. 2014, A&A, 572, A70
Roth, N. X., Gibb, E. L., Bonev, B. P., et al. 2017, AJ, 153, 168
Roth, N. X., Gibb, E. L., Bonev, B. P., et al. 2018, AJ, 156, 251
Roth, N. X., Milam, S. N., Cordiner, M. A., et al. 2021, ApJ, 921, 14
Rubin, M., Altwegg, K., Balsiger, H., et al. 2019, MNRAS, 489, 594
Saki, M., Gibb, E. L., Bonev, B. P., et al. 2021, AJ, 162, 145

Salinas, V. N., Hogerheijde, M. R., Bergin, E. A., et al. 2016, A&A, 591, A122
Song, L., & Kästner, J. 2017, ApJ, 850, 118
Taquet, V., López-Sepulcre, A., Ceccarelli, C., et al. 2015, ApJ, 804, 81
Tinacci, L., Germain, A., Pantaleone, S., et al. 2022, ESC, 6, 1514
van der Marel, N., Booth, A. S., Leemker, M., van Dishoeck, E. F., & Ohashi, S. 2021, A&A, 651, L5
van't Hoff, M. L. R., Tobin, J. J., Trapman, L., et al. 2018, ApJL, 864, L23
Villanueva, G. L., Liuzzi, G., Faggi, S., et al. 2022, Fundamentals of the Planetary Spectrum Generator (Greenbelt, MD: NASA Goddard Space Flight Center)
Villanueva, G. L., Mumma, M. J., DiSanti, M. A., et al. 2011, Icar, 216, 227
Villanueva, G. L., Smith, M. D., Protopapa, S., Faggi, S., & Mandell, A. M. 2018, JQSRT, 217, 86
Virtanen, P., Gommers, R., Oliphant, T. E., et al. 2020, NatMe, 17, 261
Walsh, C., Loomis, R. A., Öberg, K. I., et al. 2016, ApJL, 823, L10
Walsh, C., Millar, T. J., Nomura, H., et al. 2014, A&A, 563, A33
Watanabe, N., & Kouchi, A. 2002, ApJL, 571, L173
Wilson, T. L., & Rood, R. 1994, ARA&A, 32, 191
Yamato, Y., Furuya, K., Aikawa, Y., et al. 2022, ApJ, 941, 75